Doping bioactive elements into a collagen scaffold based on synchronous self-assembly/mineralization for bone tissue engineering

Huanhuan Liu[a,1], Mingli Lin[b,1], Xue Liu[a], Ye Zhang[a], Yuyu Luo[c], Yanyun Pang[a], Haitao Chen[a], Dongwang Zhu[a], Xue Zhong[a], Shiqing Ma[a], Yanhong Zhao[a], Qiang Yang[d,**], Xu Zhang[a,e,*]

[a] *School of Stomatology, Hospital of Stomatology, Tianjin Medical University, Tianjin, 300070, China*
[b] *Department of Stomatology, Zhongshan Hospital of Xiamen University, Xiamen, Fujian, 361004, China*
[c] *The Third Central Clinical College of Tianjin Medical University, Tianjin, 300170, China*
[d] *Department of Spine Surgery, Tianjin Hospital, Tianjin, 300211, China*
[e] *Institute of Stomatology, Tianjin Medical University, Tianjin, 300070, China*

ARTICLE INFO

ABSTRACT

Pure collagen is biocompatible but lacks inherent osteoinductive, osteoimmunomodulatory and antibacterial activities. To obtain collagen with these characteristics, we developed a novel methodology of doping bioactive elements into collagen through the synchronous self-assembly/mineralization (SSM) of collagen. In the SSM model, amorphous mineral nanoparticles (AMN) (amorphous $SrCO_3$, amorphous Ag_3PO_4, etc.) stabilized by the polyampholyte, carboxymethyl chitosan (CMC), and collagen molecules were the primary components under acidic conditions. As the pH gradually increased, intrafibrillar mineralization occurred via the self-adaptive interaction between the AMNs and the collagen microfibrils, which were self-assembling; the AMNs wrapped around the microfibrils became situated in the gap zones of collagen and finally transformed into crystals. Sr-doped collagen scaffolds (Sr-CS) promoted *in vitro* cell proliferation and osteogenic differentiation of rat bone marrow mesenchymal stromal cells (rBMSCs) and synergistically improved osteogenesis of rBMSCs by altering the macrophage response. Ag-doped collagen scaffolds (Ag-CS) exhibited *in vitro* antibacterial effects on *S. aureus*, as well as cell/tissue compatibility. Moreover, Sr-CS implanted into the calvarial defect of a rat resulted in improved bone regeneration. Therefore, the SSM model is a de novo synthetic strategy for doping bioactive elements into collagen, and can be used to fabricate multifunctional collagen scaffolds to meet the clinical challenges of encouraging osteogenesis, boosting the immune response and fighting severe infection in bone defects.

1. Introduction

During the development of bone or dentine *in vivo*, self-assembly of the collagen matrix is thought to precede mineralization [1]. Thus far, *in vitro* intrafibrillar mineralization of collagen has been generally achieved via the model of mineralization following self-assembly (MFS), in which collagen is completely self-assembled [2], and then, amorphous calcium phosphate (ACP) stabilized by polyelectrolytes as analogues of non-collagen proteins (NCPs) enters the collagen fibrils via gap zones [3–8]. The conceivable mechanisms in this model could involve size exclusion [9,10], capillary forces [11], electrostatic interactions [3,12] or a balance between osmotic equilibrium and electroneutrality [8]. Particularly, *in vivo* and *in vitro* studies of amelogenin inducing mineralization support a recently developed concept of templated mineralization in which the formation of an organic template and mineralization begin simultaneously in a cooperative self-assembly process of amorphous primary particles and organic macromolecules [13,14]. Therefore, it is natural to raise the question of whether collagen could be intrafibrillarly mineralized via synchronous self-assembly/mineralization (SSM), which could be exploited to develop a new collagen scaffold.

Since collagen molecules start to self-assemble in the initial acidic

---

Scheme 1. Flow diagram of the experimental procedure.

environment *in vitro*, finding the analogues of NCPs that stabilize amorphous mineral nanoparticles (AMN) under acidic conditions is key to achieve the synchronous self-assembly/mineralization of collagen (SSM model). Fortunately, our previous study indicated that CMC, a polyampholyte, has both carboxyl and amino groups and can therefore act as an anionic or cationic polyelectrolyte below or above its isoelectric point (IP = 3.5), respectively [15,16]. The SSM process starts at pH 2, and as the pH gradually increases, collagen fibrils begin to self-assemble from collagen molecules. Simultaneously, collagen microfibrils may wrap around the ACP nanoparticles and orient them in the gap zones of collagen, after which collagen fibrils with embedded ACP nanoparticles form [3]. Finally, the ACP nanoparticles transform into hydroxyapatite (HAP) crystals along the pores between collagen microfibrils to achieve intrafibrillar mineralization. Moreover, amorphous carbonate mineral MCO_3(M = Ca, Sr, Mg, Ba, Mn, Cd, Pb) nanoparticles have been generated through polymer-induced liquid-precursor (PILP) processes or synthesized in ethanol solutions [17].

Typically, strontium (Sr) has been demonstrated to facilitate the osteogenic differentiation of mesenchymal stem cells (MSCs) through the upregulation of extracellular matrix (ECM) gene expression and activation of the Wnt/β-catenin pathway. In addition, strontium can regulate the local immune microenvironment by manipulating macrophage polarization [18–21]. Thus, Sr has been doped into implant materials such as HAP, to enhance osteoinductivity [22]. In addition, silver, which exhibits antimicrobial activity by disrupting bacterial cell membranes, and binding to microbial DNA and the sulfhydryl groups of bacterial metabolic enzymes, has been incorporated into different natural and synthetic polymers including cellulose, chitosan, PCL, gelatin [23,24]. Therefore, it would make sense to develop multifunctional collagen scaffolds modified with bioactive elements possessing osteoinductive, osteoimmunomodulatory and antibacterial abilities. These studies motivated us to apply CMC to stabilize various carbonates or phosphates under acidic conditions, thereby introducing bioactive elements into collagen scaffolds via the SSM model.

The strategies for incorporating bioactive elements into collagen scaffolds mainly include direct mixing of inorganic materials with self-assembled collagen [25], one-step collagen fibril self-assembly and mineral precipitation [26], and intrafibrillar mineralization via a collagen-based MFS model [27,28]. Simple mixing of inorganic materials with self-assembled collagen could not achieve intrafibrillar mineralization [29]. Such an extrafibrillar combination of minerals and collagen is fragile, leading to the burst release of its constituent ions. Thus, to enable the sustained release of ions, intrafibrillar mineralization should be used to introduce bioactive ions into collagen.

The efficacy of intrafibrillar mineralization in the MFS model is affected by the size of mineral nanoparticles and their aggregation degree due to the size exclusion mechanism involved [9,10,30]. In addition, the aggregate of mineralized particles on the outer surface of the scaffold in the MFS model could obstruct the diffusion of mineral nanoparticles and ions into the scaffold interior, thus depressing the degree of internal mineralization.

In contrast, the SSM model involves the de novo synthesis of collagen scaffolds because all components are primary under acidic conditions. With the SSM model, it is possible to design and develop multifunctional collagen scaffolds by doping a range of amorphous minerals containing bioactive elements into collagen fibrils for bone regeneration. Herein, we hypothesized that positively charged CMC could stabilize nanoparticles (including amorphous strontium carbonate, amorphous silver phosphate, etc.) under acidic conditions, and that these amorphous mineral nanoparticles could be introduced into collagen fibrils via the SSM model. Accordingly, osteogenesis and immunomodulation of Sr-doped collagen scaffolds (Sr-CS) and antibacterial activity of Ag-doped collagen scaffolds (Ag-CS) were investigated.

2. Materials and methods

To better epitomize the experimental procedure, a flow diagram is shown in Scheme 1 with all steps involved.

2.1. Materials

CMC and glacial acetic acid were purchased from Life Science Products & Services (Shanghai, China). Other chemicals, including strontium chloride hexahydrate ($SrCl_2 \cdot 6H_2O$), magnesium chloride dihydrate ($MgCl_2 \cdot 2H_2O$), zinc chloride ($ZnCl_2$), ferric chloride ($FeCl_3$), copper nitrate ($Cu(NO_3)_2$), silver nitrate ($AgNO_3$), dipotassium hydrogen phosphate (K_2HPO_4), sodium carbonate (Na_2CO_3), hydrochloric acid (HCl), sodium hydroxide (NaOH), 1-ethyl-3-(3-dimethylamino-propyl)-carbodiimide (EDC), N-hydroxysuccinimide (NHS), Tris-HCl-NaCl buffer, phosphate-buffered saline (PBS), and HEPES buffer (pH = 7.2–7.4, sterilized), were all purchased from Sigma-Aldrich (Beijing, China) and used as received. Foetal bovine serum (FBS), Dulbecco's Modified Eagle's Medium (DMEM), and penicillin/streptomycin were purchased from Sigma-Aldrich Co. (St. Louis, MO, USA). The alkaline phosphatase (ALP) assay, Cell Counting Kit-8(CCK-8) and live/dead cell double staining kits were purchased from Solarbio (Beijing, China). Haematoxylin and eosin (H&E) and Masson's trichrome stain kits were purchased from Muto Pure Chemicals Co. Ltd., Japan.

2.2. Preparation of type I collagen

Rat tail tendon fascicles extracted from Sprague-Dawley (SD) rats (7 weeks old) were dissolved in Tris-HCl-NaCl buffer (0.05 M, pH 7.4) for 24 h and then dissolved in acetic acid (0.03 mol/L) with stirring for two days. Next, the collagen solution was centrifuged (3000 rpm) for 30 min at 4 °C. The precipitation was collected in sterile centrifuge tubes and stored at 4 °C.

2.3. Preparation and characterization of CMC-AMN solutions

The CMC solution was prepared by dissolving 200 mg of CMC powder into 30 mL of deionized water with stirring (1000 rpm) for 15 min until the CMC powder was fully dissolved. The pH was adjusted to approximately 2 using 1 mol/L HCl at room temperature. Then, 0.168 g of $SrCl_2 6H_2O$ was dissolved in 10 mL of deionized water, and this solution was added dropwise to the CMC solution. Next, 0.026 g of Na_2CO_3 was added dropwise to the CMC solution with stirring (500 rpm) for 5 min to form a well-proportioned and stable CMC/amorphous strontium carbonate (ASC) solution. The final concentrations of Sr^{2+} and CO_3^{2-} were 10 mM and 6 mM, respectively. Other CMC/AMN solutions were prepared in a similar way, and the chemical compositions are shown in Table 1. Samples of the CMC/AMN solutions for transmission electron microscopy (TEM)/selected-area electron diffraction (SAED) characterization were prepared by dropping the solutions onto 400-mesh copper grids covered by carbon support film, after which the grids were air-dried at room temperature. These unstained samples were examined using a JEM-1230 system operating at 110 kV (JEOL Tokyo, Japan). SAED was used to determine the crystallinity of the minerals. The particle size distribution of the nanoparticles was characterized using a Zetasizer Nano ZS (Malvern Instruments, Westborough, MA, USA). Zeta potential measurements of

Table 1
Recipes of preparation for amorphous mineral nanoparticles.

Inorganic mineral	Amount	K_2HPO_4 (mg)	Na_2CO_3 (mg)	Concentration Ratio
$SrCl_2 \cdot 6H_2O$	106.61 mg		25.44	10:6
$MgCl_2 \cdot 2H_2O$	38.09 mg		25.44	10:6
$ZnCl_2$	13.63 mg	10.44		2.5:1.5
$FeCl_3$	27.03 mg	10.44		2.5:1.5
$Cu(NO_3)_2$	12.08 mg	5.22		1.25: 0.75
$AgNO_3$ (1 mol/L)	0.125 mL	5.22		1.25: 0.75

CMC/AMN stabilized solutions were performed using a Malvern Nano ZS system (Malvern, England).

2.4. Preparation and characterization of pure collagen scaffold and bioactive element-doped collagen scaffold (BE-CS)

To fabricate the pure collagen scaffold, type I collagen was placed in a dialysis bag (8000-14,000 Da) immersed in 15 mL of PBS for 2 days. Then, a 1-mm-thick and 10-mm-diameter mould was used to set the collagen hydrogel for lyophilization.

Incorporation of Sr^{2+}/Ag^{+} into collagen was achieved using synchronous self-assembly/mineralization of collagen (SSM) by mixing the acidic CMC-stabilized nanocomposite solution with the acid-dissolved type I collagen in a dialysis bag at a volume ratio of 3:1. The dialysis bags were then immersed in 15 mL of PBS buffer (0.01 mol/L, pH 6.8–7.4) for 2 days (changing the buffer each day) as the solution pH in the bags decreased to approximately 6.0. Next, the solution pH in the dialysis bags was adjusted to approximately 7.0–8.0 by adding drops of NaOH (1 M) to facilitate the transformation of the amorphous minerals to crystals. Finally, the dialysis bags were placed in 15 mL of HEPES buffer (10 mM) for 2 days (changing the buffer each day). The samples for TEM/SAED characterization were prepared by dropping the self-assembled collagen gel doped with bioactive elements on 400-mesh copper grids covered with carbon support film, and the gel layer was thinned by air-blowing; the grids were then air-dried at room temperature. These unstained samples were examined using a JEM-1230 system operating at 110 kV.

Porous 3D scaffolds of bioactive element-doped collagen were prepared by 24 h of lyophilization of the collagen gel collected by centrifugation (3000 rpm, 5 min). Before lyophilization, the collagen gel was cross-linked with a solution of EDC and NHS (3:1) for 24 h in Teflon moulds, which tailored the shape of the scaffolds.

The attenuated total reflectance-Fourier transform infrared (ATR-FTIR) spectra of the collagen scaffolds were recorded in reflection mode using an infrared spectrophotometer (Shimadzu 8400S, Japan). Spectra were collected from 700 to 4000 cm^{-1} at a resolution of 16 cm^{-1} with 100 scans each.

The morphology and structure of scaffolds were characterized using scanning electron microscopy (SEM, JSM-6701F, JEOL, Japan) at 15 kV. Energy-dispersive (EDX) spectroscopy (Inca X-Max, UK) was applied to determine the elemental distribution in the scaffolds. Before the observations, the samples were sputter-coated with gold using a sputter coater in an argon atmosphere.

Thermogravimetric analysis (TGA) was performed with a Q5000 thermogravimetric analyser (TA Instruments, New Castle, DE, USA) in a nitrogen atmosphere by heating to 1000 °C at a rate of 20 °C/min. Inductively coupled plasma-atomic emission spectroscopy (ICP-AES, PE-7000DV, USA) was applied to detect the trace elements released from the scaffolds.

2.5. Sustained release of strontium ions and silver ions

To investigate the release profiles of Sr^{2+} and Ag^{+}, Sr-CS and Ag-CS (5 mg) were soaked in 10 mL of PBS (pH 7.2, 0.01 M) and incubated at 37 °C for 21 days. On days 7, 14, and 21, the supernatant was collected after centrifugation to determine the *in vitro* ion release using ICP-AES. Three parallel measurements were conducted for averaging. To ensure continued release, the PBS in the system was replenished, and the samples were maintained at 37 °C.

2.6. Cell culture

SD rat bone marrow mesenchymal stromal cells (rBMSCs) and murine-derived macrophages (RAW264.7 cells) were used in the *in vitro* study. rBMSCs and RAW264.7 cells were purchased from Cyagen Biosciences (Guangzhou, China). Both cells types were incubated in

DMEM supplemented with 10% FBS and 1% (v/v) penicillin/strepto-mycin at 37 ˚C in a humidified atmosphere with 5% CO_2. For the os-teogenic differentiation of rBMSCs, inductive medium was prepared by adding 50 μmol/L ascorbate (Sigma, USA), 10 mmol/L β-glyceropho-sphate (Sigma, USA) and 100 nmol/L dexamethasone (Sigma, USA). The media were refreshed every day in all cases. Prior to rBMSC seeding, the scaffolds were cut into discs with a diameter of 15 mm to match the well size of a 24-well plate, and sterilized with a 25-kGy dose of gamma radiation (cobalt-60) as a reference (Huanming Gaoke Fuzhao Co., China) [31].

2.7. Cell viability

Cell proliferation on different scaffolds against rBMSCs was ana-lysed using the CCK-8 kit. The strontium-doped and pure collagen scaffolds (Sr-CS, Ag-CS and CS samples) were pre-wetted with complete growth medium. Then, 1×10^4 rBMSCs in 1 mL of medium were seeded onto sterilized scaffold disks (n = 3) placed in 24-well plates. On days 1, 3, 5, and 7, CCK-8 solution (10% in fresh medium) was added to each well of the 24-well plates to replace the original culture medium and then incubated at 37 ˚C in 5% CO_2 for 3 h. Subsequently, the supernatant solution was transferred to a 96-well plate, and the optical density (OD) of the incubated solution was measured at 450 nm using a microplate reader (RT-6000; Rayto, Guangdong, China).

For the live/dead staining assay, on days 1, 3, 5, and 7, after the cells were seeded onto the Sr-CS, Ag-CS and CS samples, the cell/scaffold complexes were treated with acridine orange and ethidium bromide (AO/EB) (Life Technologies Corporation, Carlsbad, CA), and fluorescence images were captured using confocal laser scanning mi-croscopy (CLSM, TCS SP5, Leica, Germany). For cell morphology eva-luation, after 3 days, the samples were stained with Alexa Fluor 546-phalloidin (Sigma-Aldrich) to label the cytoskeleton and mounted with mounting medium containing 4′,6-diamidino-2-phenylindole (DAPI) for nucleus staining, and fluorescence images were captured by CLSM.

2.8. In vitro differentiation study

On days 7 and 14, ALP activity was determined in the strontium-doped and pure collagen scaffolds. In a 24-well culture plate, 1 mL of the rBMSC suspension was seeded on each specimen at a density of 1×10^4 cells per well, and the culture medium was replaced with os-teoinductive medium after 24 h of cell adhesion. To prepare cell lysates for quantitative analysis, cell lysis buffer (1 mL) containing 1% Triton X-100, 20 mmol/L Tris and 150 mM NaCl was added in sequence to every well, followed by three freeze-thaw cycles and centrifugation. After the ALP assay (Sigma Life Sciences, USA), quantification was performed by measuring the absorbance at 520 nm with a microplate reader according to the manufacturer's protocol. For quantitative real-time polymerase chain reaction (RT-PCR) analysis, total cellular RNA was isolated from cells cultured on each scaffold using a TRIzol RNA extraction kit (Gibco, USA) and then reverse-transcribed into cDNA using a Revert Aid First-Strand cDNA Synthesis kit (Thermo Fisher Scientific, USA) according to the manufacturer's instructions. Three genes related to osteogenesis, namely, RUNX2 and osteocalcin (OCN), ALP, were selected. PCR was performed using a QuantiTect SYBR Green PCR kit (Roche, Basel, Switzerland) and an Applied Biosystems 7500 system (Thermo Fisher Scientific). The primer sequences for the genes are listed in Table 2.

2.9. Response of macrophage on the prepared scaffolds

RAW264.7 cells were seeded on the scaffolds in 24-well plates $(1 \times 10^4/\text{well})$. After 3 days of cultivation, the culture medium was collected and centrifuged at 4 ˚C to obtain the supernatants, which were mixed with fresh complete DMEM at a ratio of 1:2 to generate macro-phage-conditioned materials for subsequent experiments. The

Table 2
Primers sequences used for RT-PCR of BMSCs.

Gene	Forward primer sequence (5′-3′)	Reverse primer sequence (5′-3′)
RUNX2	GCACCAGCCCATAATAGA	TTGGAGCAAGGAGAACCC
OCN	GGTGCAGACCTAGCAGACACCA	AGGTAGCGCCGGAGTCTATTCA
ALP	AACGTGGCCAAGAACATCATCA	TGTCCATCTCCAGCCGTGTC
GAPDH	CGTCTTCACCACCATGGAGA	CGGCCATCGCCAGTTT

RUNX2, runt-related transcription factor 2; OCN, osteocalcin; ALP, alkaline phosphatase; GAPDH, glyceraldehydes-3-phosphate dehydrogenase.

Table 3
Primers sequences used for RT-PCR of RAW264.7

Gene	Forward primer sequence (5′-3′)	Reverse primer sequence (5′-3′)
TNF-α	ACTGAACTTCGGGGTGATCG	TGTCTTTGAGATCCATGCCGT
IL-6	CATGTTCTCTGGGAAATCGTGG	TCCAGGTAGCTATGGTACTCC
IL-10	CTCCTAGAGCTGCGGACTG	GCTCCTTGATTTCTGGGCCAT
BMP2	TGCTAGATCTGTACCGCAGG	TCTGTTCCCGGAAGATCTGG
TGFβ1	CAGTACAGCAAGGTCCTTGC	ACGTAGTAGACGATGGGCAG
GAPDH	GGGTCCCAGCTTAGGTTCATC	TGCCGTGAGTGGAGTCATAC

TNF-α, tumor necrosis factor α; IL-6, interleukin-6; IL-10, interleukin-10; BMP2, bone morphogenetic protein 2; TGFβ1, transforming growth factor β1; GAPDH, glyceraldehydes-3-pgosphate dehydrogenase.

polarization of RAW264.7 cells was evaluated by RT-PCR (as described earlier). The RT-PCR primers are listed in Table 3.

2.10. Response of rBMSCs to macrophage-conditioned medium

To investigate the effect of macrophages on the osteogenesis of rBMSCs, RAW cell culture supernatants were used as the conditioned medium to stimulate rBMSCs. rBMSCs were cultured at a density of 1×10^4 cells with conditioned medium. On days 7, and 14, ALP ac-tivity was assayed. Total RNA was harvested, and gene expression as-says were performed by RT-PCR. The osteogenesis-related genes were RUNX2, OCN and ALP, as described earlier.

2.11. Incubation of bacteria with the scaffolds

The potential antibacterial activity of Ag-CS was evaluated by in-cubating *Staphylococcus aureus* (*S. aureus*, ATCC 25923) with different scaffolds. *S. aureus* ATCC 25923 was purchased from the American Type Culture Collection (ATCC, VA, USA) and incubated in brain heart in-fusion (BHI, Solarbio) broth in an anaerobic chamber (N_2: 80%, H_2: 10%, CO_2: 10%) at 37 ˚C. The *S. aureus* suspension was diluted to a concentration of 10^5 CFU/mL (CFU, colony forming units) for the an-tibacterial assay. Sterilized scaffold samples (n = 3) were pre-wetted with BHI, placed in 24-well culture plates with 1 mL of *S. aureus* sus-pension, and cultured at 37 ˚C in an anaerobic chamber incubator.

2.12. Antibacterial effects of Ag-CS

The antibacterial activity of Ag-CS was evaluated using serial dilu-tions and the spread plate method. At different intervals (24 h, 48 h, and 72 h), the scaffolds were moved, gently rinsed with PBS to elim-inate non-attached bacteria, and then ultrasonically treated at 40 W for 5 min in a new 24-well plate filled with 1 mL of BHI per well, Then, the bacterial suspensions were sampled to count the viable bacteria ad-hered to the scaffolds. During the incubation period, the bacterial sus-pension medium was replaced with new culture medium daily. The antibacterial efficacy of samples against adhered bacteria was de-termined by the following formula: $R = (B-A)/B \times 100\%$, where A is the average number of viable bacteria on a silver-doped scaffold sur-face, and B is the average number of viable bacteria on a blank scaffold surface. At predetermined time points (24 h, 48 h, and 72 h), the

samples were prefixed with phosphate-buffered 2.5% glutaraldehyde (BioChemika, Fluka), rinsed with PBS three times and observed by SEM. After incubation for 3 days, live/dead staining was conducted using an AO/EB staining kit, and fluorescence images were recorded by CLSM.

2.13. Calvarial defect model

The Institutional Ethics Committee of Tianjin Medical University approved the use of SD rats for the experiments conducted in this study. The sixty male SD rats (200–250 mg) used to establish the calvarial defect model for the *in vivo* study were divided into 3 groups (15 rats per group) and treated as follows: (1) the defect was left unfilled (control group); (2) the defect was filled with pure collagen scaffolds (CS group); and (3) the defect was filled with Sr-CS (Sr-CS group). Briefly, the rats were anaesthetized by intraperitoneal injection of chloral hydrate (1 mg/330 g; Yulong, Yangshuo, China). After exposure of the parietal calvarium, a full-thickness skull defect (5 mm in diameter) was prepared with a trephine bur, which was cooled by continuously dripped sterile saline. After the scaffolds were filled into the defects, the overlying tissue was closed with sutures using a 5-0 suture line. At 4, 8, 12, and 24 weeks post-surgery, the three groups of rats were sacrificed by injection of an overdose sodium of pentobarbital. Retrieved skulls were fixed in formalin overnight for further investigations.

2.14. Characterization of bone regeneration

Micro-CT scans were performed to assess the 3D collagen scaffolds and new bone formation using a micro-CT scanner (Sky Scan 1174v2, SkyScan N.V., Kontich, Belgium). A 5 mm-diameter circular region was selected in the centre of the calvarial defect area to perpendicularly locate the cylindrical volume of interest for analysis. Reconstruction of the projection image and calculation of bone volume (grey value > 1000) were performed using NRecon software v.1.6.9 (Bruker micro-CT).

After micro-CT analysis, the isolated specimens were decalcified in 10% EDTA for 8 weeks, followed by dehydration and embedding in paraffin. In the centre of the bone defects, 5-μm serial transverse sections were prepared for histological analysis. Three randomly-selected cross-sections from each sample were stained with H&E and Masson's trichrome (Baso Diagnostics Inc., Zhuhai, China). All images were captured with digital slice scanning equipment (Nanozoomer, Hamamatsu, Japan).

2.15. Statistical analysis

The experiments were repeated 3 times to ensure the validity of the evaluation, and all data are expressed as the mean ± SD. Significant differences were identified using one-way ANOVA with a post hoc least significant difference (LSD) test and Student-Newman-Keuls (SNK) test. A value of $*P < 0.05$ was considered significant, and $**P < 0.01$ was considered highly significant.

3. Results

3.1. Characterization of the amorphous mineral nanoparticles

The various nanoparticles composed of amorphous minerals containing Sr^{2+}, Mg^{2+}, Zn^{2+}, Fe^{3+}, Cu^{2+}, and Ag^+ could be stabilized by CMC at pH 2, and the emulsified state of the mineral solutions could be maintained for at least 24 h (Supporting Information S1). By contrast, at pH 7, the emulsified state of the mineral solutions could be stabilized for a maximum of 24 h. The morphology of CMC/ASC and CMC/ASP nanoparticles at is shown in Fig. 1d, g, and their amorphous phase was characterized by SAED. The morphology of the other CMC/AMN is presented in Supporting Information S2. The mean diameter of the

CMC/AMN was approximately 35–300 nm based on dynamic light scattering (DLS) measurements (Supporting Information S3). The zeta potential of nanoparticles stabilized by 5 mg/mL CMC at pH 2 was found to be positive (Supporting Information S4).

3.2. Fabrication and characterization of scaffolds

A series of time-resolved analyses were conducted to investigate the SSM and MFS modes of mineralization using unstained samples. For the MFS model, most ASC nanoparticles (Fig. 1a) only coated the surfaces of the collagen fibrils after 3 days (Fig. 1b and c). Interestingly, during SSM, an image of collagen fibrils simultaneously in the pre-assembly and post-assembly scenes was captured after 24 h of mineralization, and the co-occurrence of collagen microfibrils and ASC nanoparticles is shown in the pre-assembly image (Fig. 1d and e). The spindle-shaped mineral nanoparticles with a length of approximately 40 nm corresponding to the gap region of collagen were orderly arranged along the long axes of the fibrils (Fig. 1f). Moreover, the relationship between ASP nanoparticles (Fig. 1g) and collagen fibres was similar to the process observed for ASC nanoparticles (Fig. 1h and i). Finally, the mineral crystals were clearly identified within the fibrils that reproduced the cross-banding pattern, strongly indicating intrafibrillar mineralization. Other minerals with Mg^{2+}, Zn^{2+}, Fe^{3+}, and Cu^{2+} were similarly organized into arrays with their c-axes co-aligned with the long axes of the fibrils (Supporting Information S5).

The bioactive element-doped collagen scaffold was also characterized by STEM-EDX, FTIR, TGA and ICP-AES analyses. The typical Sr-CS remained highly porous with no obvious change in porosity and morphology from pure collagen scaffolds (Fig. 2). The porosity of the Sr-CS group (65.52 ± 1.95)% was not significantly different from the CS group (67.97 ± 1.44)% ($P > 0.05$). The presence of various elements within the collagen fibrils was confirmed using STEM-EDX (Supporting Information S8). FTIR was used to identify the intrafibrillar mineralization of collagen, taking the spectrum of pure collagen as a reference [32]. The amide I peak at 1654 cm^{-1} predominantly corresponded to the C=O stretch, the amide II peak at 1550 cm^{-1} to a combination of the N–H in-plane bend and the C–H stretch, and the amide III peak at 1300 cm^{-1} to a combination of the C–N stretch and the N–H in-plane bend, which are representative of collagen (Fig. 3a). The doping of various minerals into collagen resulted in a decrease in the intensity of the amide I, II, and III bands. These phenomena could be attributed to the interaction of the mineral cations with the carboxyl or carbonyl groups of collagen [33].

The TGA results showed various mineral concentrations in the scaffolds fabricated using the SSM model (Supporting Information S9). ICP-AES was used to quantitatively investigate the composition of the scaffolds. The SSM model achieved higher loading of elements than the MFS model (Fig. 3b). Taken together, the TGA and ICP-AES results supported the high efficacy of intrafibrillar collagen mineralization by the SSM model.

3.3. Sr^{2+} and Ag^+ release profiles

The Sr-release profiles shown in Fig. 3(c–f) indicate that the SSM model maintained a sustained release pattern (8.04–0.45 μg/mL) over 21 days, while for the MFS model, the concentration of Sr^{2+} was 5.40 μg/mL on day 1 and decreased from day 7, reaching 0.02 μg/mL on day 21. Moreover, the Ag-release profiles show that the SSM model maintained a sustained release pattern (2.66–0.16 μg/mL) over 21 days. In comparison, the concentration of Ag^+ was 2.27 μg/mL on day 1 and decreased from day 7, reaching 0.01 μg/mL on day 21. The accumulated Sr^{2+} release reached 20.91 μg/mL for SSM and 7.79 μg/mL for MFS; the accumulated Ag^+ release reached 6.97 μg/mL for SSM and 3.16 μg/mL for MFS. MFS and SSM exhibited similar release kinetics for Sr^{2+} or Ag^+ over the whole experimental period. The SSM model constantly released approximately four times the amount of ions
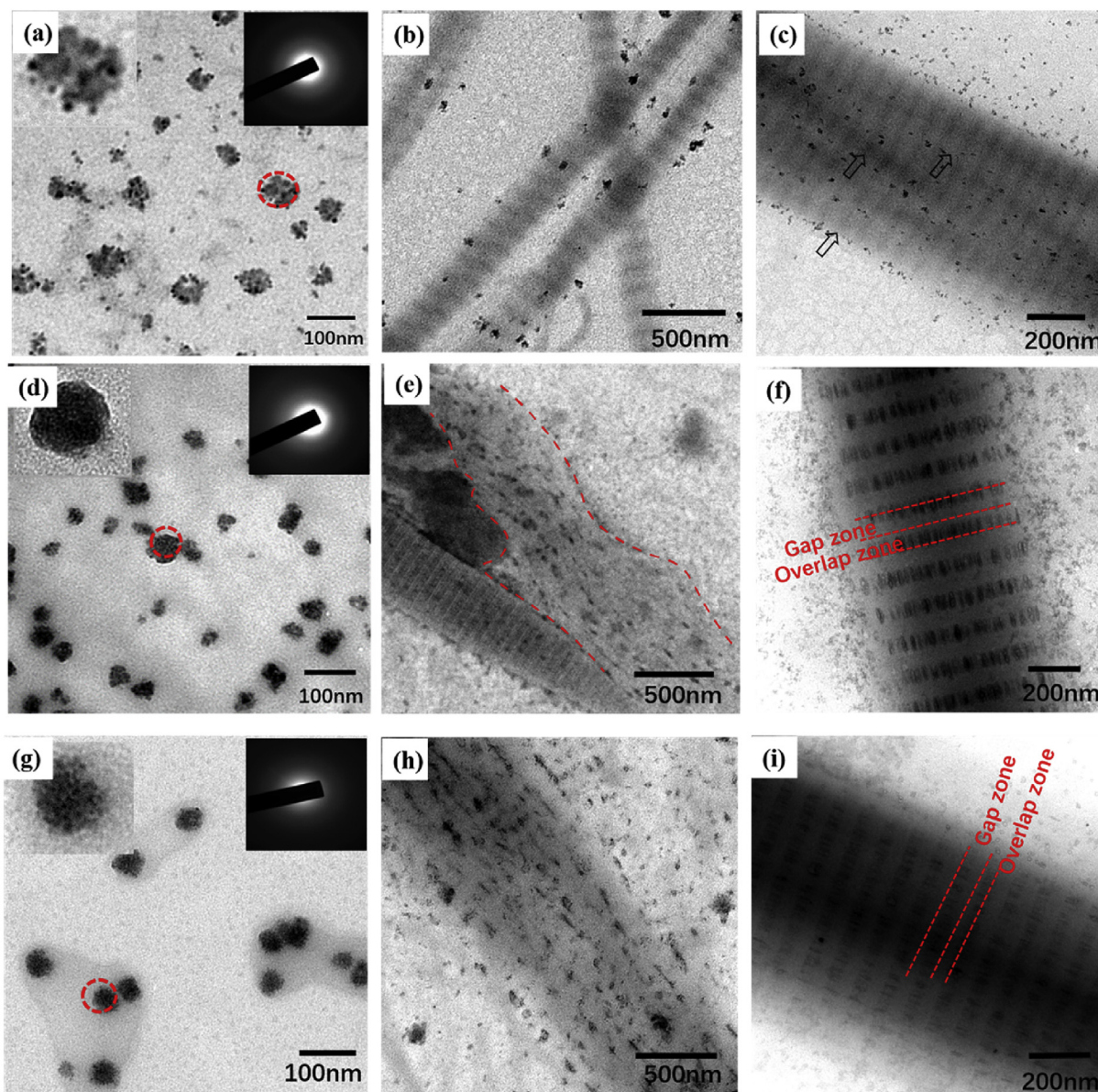
Fig. 1. (a) Low-magnification image of nanocomplexes of CMC/ASC at pH 7. Inset: High magnification of CMC/ASC and the corresponding SAED pattern indicating the amorphous phase. (b, c) Image of aggregates of ASC nanoparticles (open arrows) irregularly covering self-assembled collagen fibrils after 3 days in the MFS model. (d) Low-magnification image of CMC/ASC at pH 2. (e) Image of collagen fibrils with pre-assembly and post-assembly scenes (indicated by the red dashed line) after 24 h of mineralization in the SSM model. (f) Image of the spindle -like ASC aggregated in gap zones of the fibril and lined up along the long axis regularly after 3 days of mineralization in the SSM model. (g) Low-magnification image of CMC/ASP at pH 2. (h) Image of collagen fibrils with pre-assembly and post-assembly scenes after 24 h of mineralization in the SSM model. (i) Image of the spindle -like ASP arranged along the long axis after 3 days of mineralization in the SSM model.

compared with the MFS model, with higher cumulative concentrations corresponding to higher bioactive element loadings. These release results supported those obtained for TGA and ICP-AES, thus, compared with the MFS model, the SSM model could load more bioactive elements due to the higher efficiency of intrafibrillar mineralization.

3.4. Antibacterial activity of Ag-CS in vitro

The bactericidal and bacteriostatic activities of Ag-CS against *S. aureus* were examined by the plate count method, and the inhibition ratio was evaluated as the antimicrobial efficiency (Fig. 4a). The Ag-CS group exhibited stronger antibacterial activity against *S. aureus* than the CS group at 72 h ($P < 0.05$), which was supported by the SEM images (Fig. 4c). To determine the viability of the bacteria on Ag-CS, the adherent cells were stained with the fluorescent live/dead viability kit before CLSM observation (Fig. 4b). Incorporating silver into collagen is

an effective method to impart scaffolds with antibacterial properties.

3.5. Assays of the cytotoxicity of Sr-CS and Ag-CS

To show the potential for practical biomedical use, we investigated the biocompatibility of Sr-CS and Ag-CS. Excellent biocompatibility is one of most important prerequisites for scaffold materials to support cell adhesion, spreading, and proliferation. After 1 day of culturing, similar levels of proliferation were observed among Sr-CS, Ag-CS, and CS, and the last group was used as the control group. Interestingly, the cell proliferation on all the samples intensified over time after rBMSCs were cultured on 24-well plates. Typically, rBMSCs cultured on Sr-CS showed better proliferation than those cultured on CS at 3, 5, and 7 days ($P < 0.05$) (Fig. 5a), while the cell proliferation on Ag-CS showed no significant difference from that on the control scaffold ($P > 0.05$). CLSM images were further used to visually evaluate the adhesion and
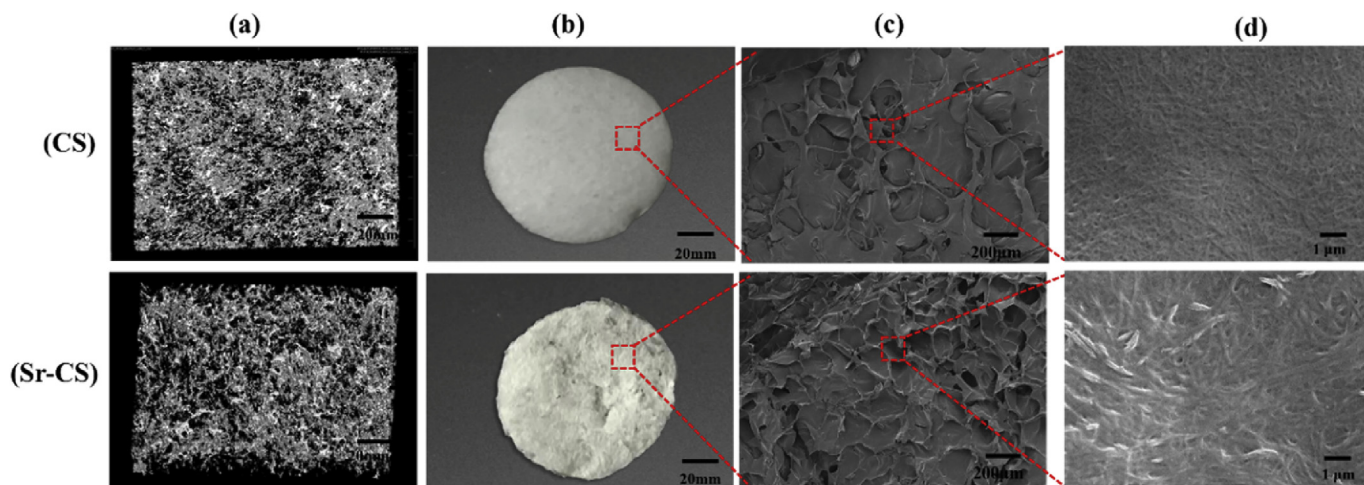
Fig. 2. (a) Micro-CT of CS and Sr-CS. (b) Images of lyophilized collagen scaffold. (c) Low-magnification SEM images of the area indicated by a rectangle with a red dashed line in (b). (d) High-magnification image of the area indicated by a rectangle with a red dashed line in (c).

morphology of rBMSCs cultured with Sr-CS and CS (Fig. 5b). The cells cultured on the two scaffolds displayed normal spindle-like shapes with oval nuclei in general, obvious lamellipodia after culture for 3 days, and a large spreading area with long and net-like lamellipodia at 5 days. These results suggested that the scaffolds were not toxic to rBMSCs and contributed to cell adhesion and proliferation.

3.6. Osteopromotive effects of Sr-CS

The osteogenic differentiation of rBMSCs on Sr-CS was evaluated by measuring the ALP activity and expression level of osteogenesis-related genes after culture for 7 and 14 days on Sr-CS and CS. In general, the ALP activity of the cells on all the samples increased over the

incubation time. At different time intervals, the relative ALP activity of the cells on the Sr-CS samples was significantly higher than on the CS samples ($P < 0.05$). In particular, the Sr-CS samples showed more noticeable osteoinductivity on day 14 (Fig. 5c). To further investigate the osteogenic effects of the various scaffolds, osteogenesis-related gene expression levels were examined by RT-PCR. The expression levels of RUNX2 and OCN in the rBMSCs on all scaffolds increased from 7 to 14 days. Notably, the gene expression levels with the Sr-CS samples were higher than those of the CS samples ($P < 0.05$) (Fig. 5d and e).
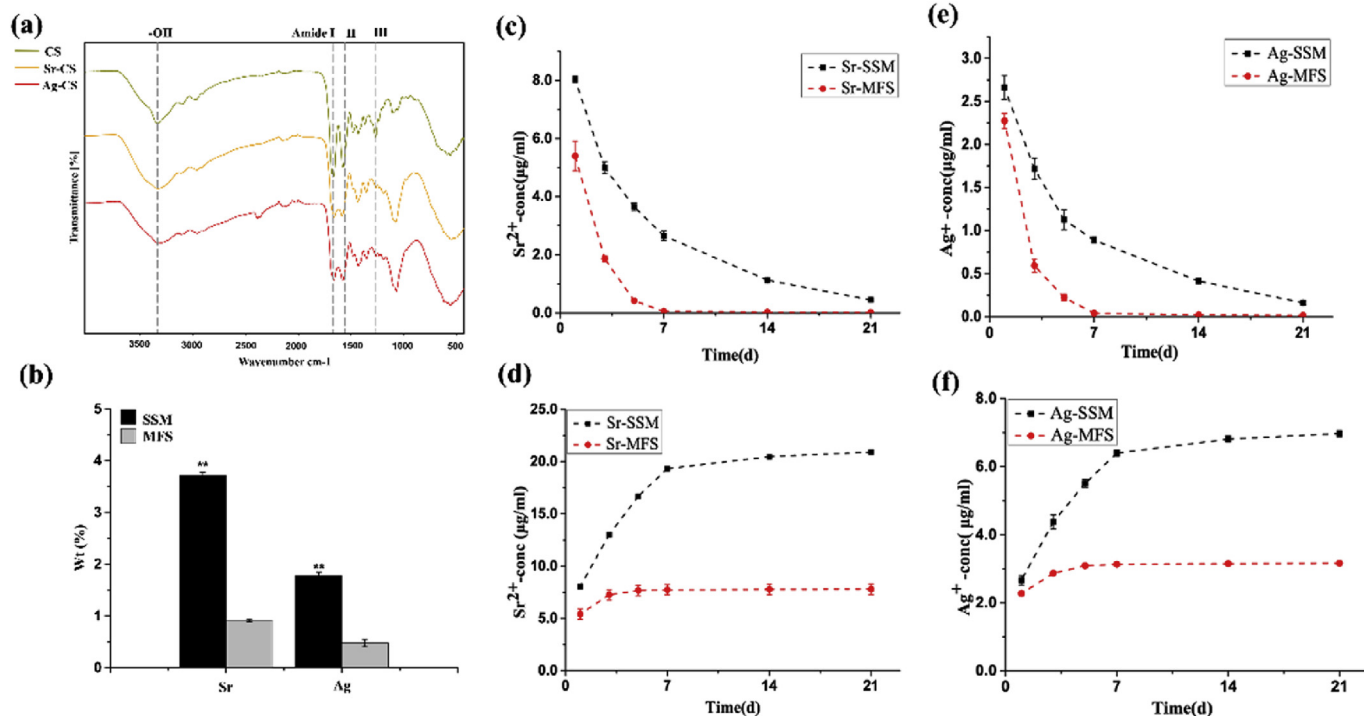

Fig. 3. (a) ATR-FTIR spectra of various scaffolds showed the typical peaks of pure collagen scaffold and decrease in the intensity of the amide I, II, and III bands in Sr-CS and Ag-CS. (b) Weight percent of various scaffolds. (n = 3, mean ± SD, **$P < 0.01$ vs CS group). (c) Absolute and (d) cumulative concentration of Sr^{2+} released from collagen scaffolds by SSM and MFS after immersion in pH 7.4 phosphate-buffered saline (PBS) for 21 days. (e) Absolute and (f) cumulative concentration of Ag^+ released in pH 7.4 phosphate-buffered saline (PBS) (n = 3; mean ± SD).
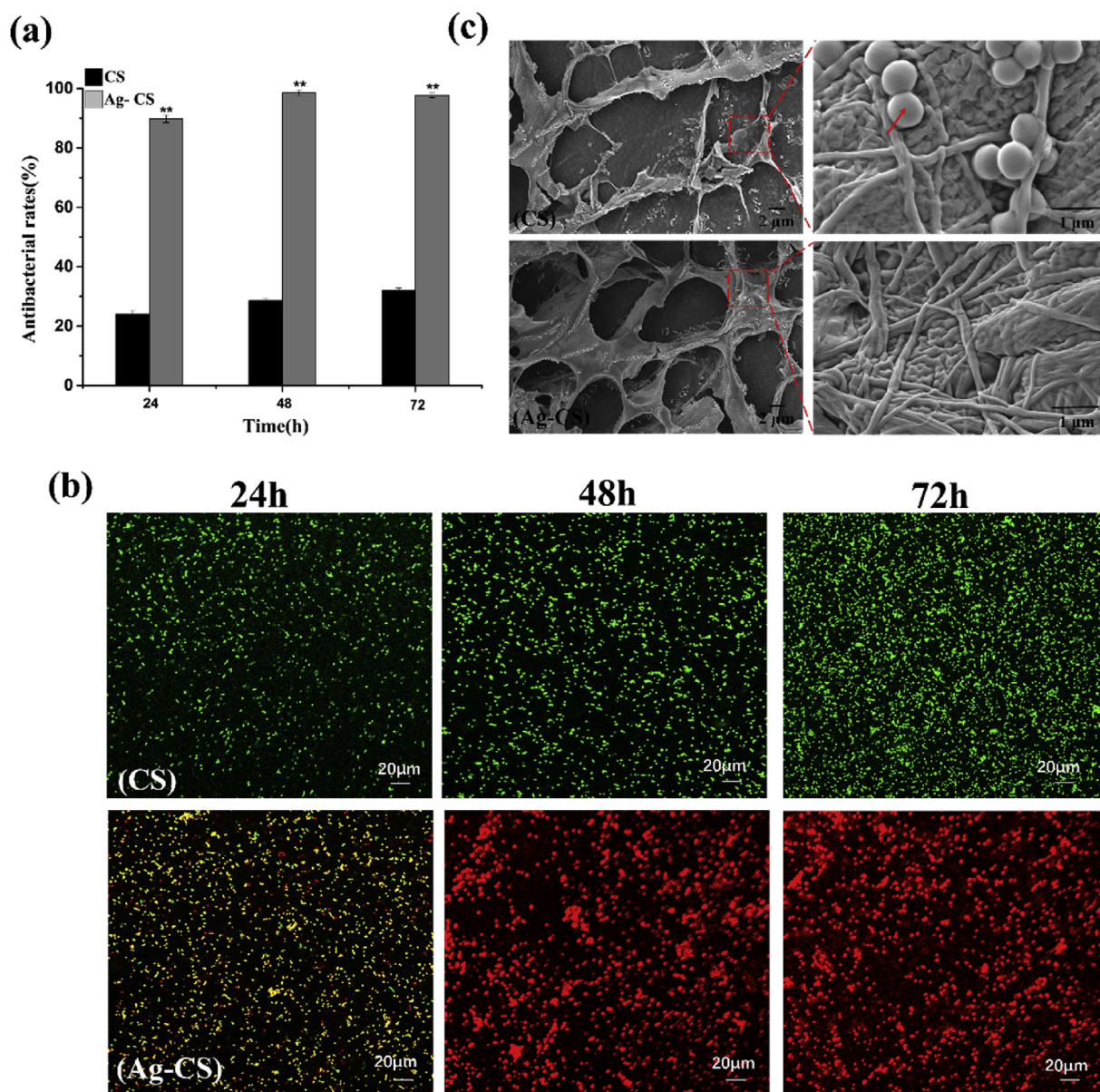
Fig. 4. (a) The antibacterial rate of pure collagen scaffolds and Ag-doped collagen scaffolds after 24 h, 48 h and 72 h (n = 3, mean ± SD, **P < 0.01 vs CS group). (b) Fluorescence microscopic inspection of CS and Ag-CS showing the viability of the bacteria on samples after 24 h, 48 h and 72 h. (c) Image showing the adherence of *S. aureus* (red arrow) on CS and Ag-CS samples.

3.7. Osteogenesis of macrophage-conditioned Sr-CS

3.7.1. Response of macrophage on the prepared scaffolds

The morphology of RAW cells cultured with Sr-CS and CS was observed by CLSM (Fig. 6a), and the results for the macrophage surface marker detected by RT-PCR showed that genes encoding pro-inflammatory cytokines, such as the inflammatory genes IL-6, IL-10 and TNF-α, were significantly downregulated in cells grown on Sr-CS compared with those grown on CS after culture for 3 days (P < 0.05). In contrast, the expression of the osteogenesis-related genes BMP2 and TGFβ1 secreted by the M2 phenotype was significantly upregulated in the Sr-CS compared with the CS group (P < 0.05) (Fig. 6b).

3.7.2. Response of rBMSCs to macrophage-conditioned medium

The results of the ALP activity assay showed that cells had a higher osteogenic output in the Sr-CS than the CS group after culture for 7 and 14 days (P < 0.01) (Fig. 6c). Compared with the expression in the CS group, the mRNA expression of mineralization-related genes (RUNX2,

OCN, ALP) in rBMSCs stimulated by Sr-doped macrophage-conditioned medium was significantly upregulated on both day 7 and day 14 (P < 0.01) (Fig. 6d and e).

3.8. Immune response and bone regeneration of Sr-CS in vivo

The Sr-CS group showed significantly greater levels of cellular viability than the CS group. Based on these results, animal tests to evaluate potential clinical applications of Sr-CS were performed. In this study, the calvarial osteogenesis animal model was utilized to assess the osteogenic capability of the materials: the materials were implanted into full-thickness skull defects (5 mm in diameter), and the formation of new bone tissues in or around the materials was investigated (Supporting Information S11). After 1, 2, 3, and 6 months of implantation, the defect areas were retrieved together with their surrounding tissues and fixed in formalin overnight for further analysis. The 3D reconstruction and micro-CT analysis of the specimens (Fig. 7) at each time point were used to assess new bone formation based on the
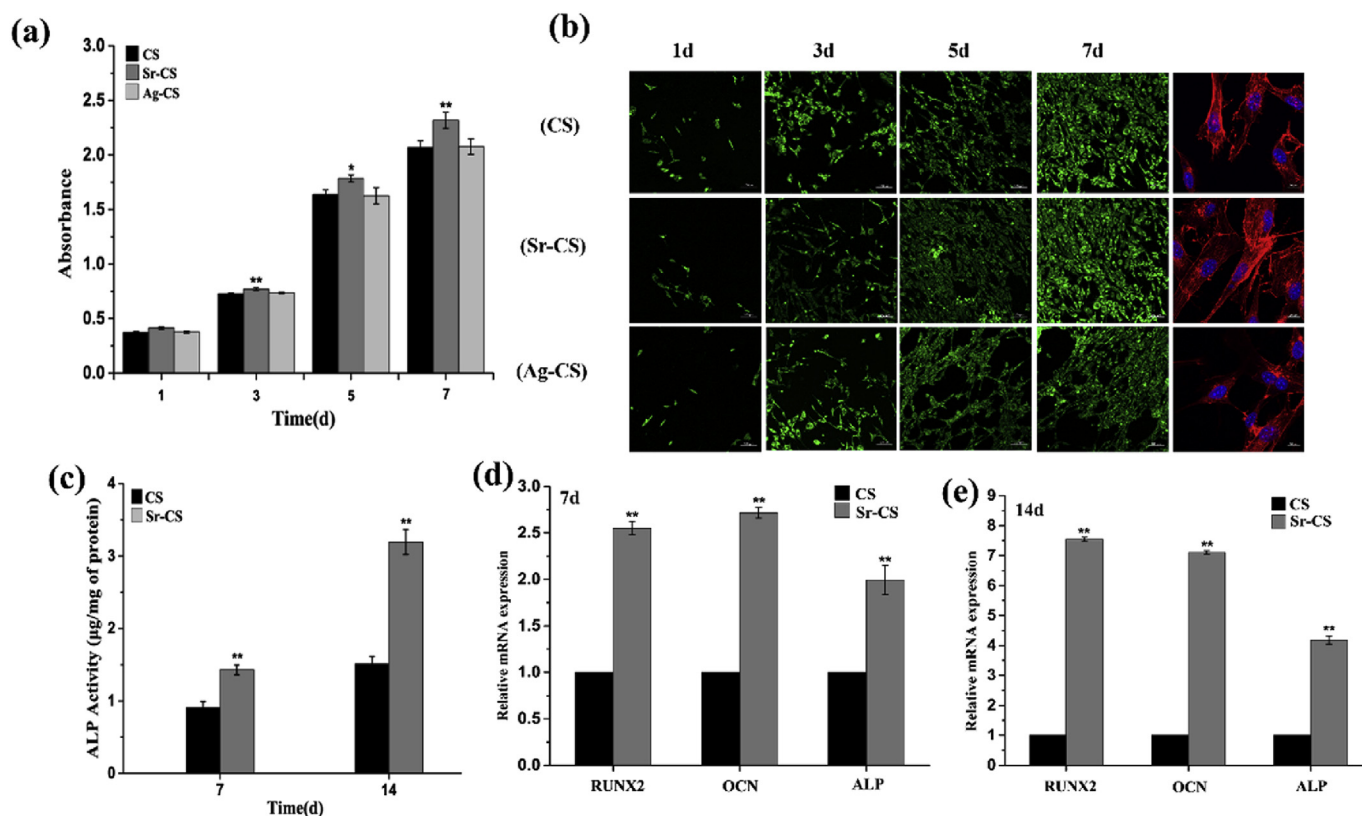
Fig. 5. (a) CCK-8 assay results of rBMSCs distributed on different collagen scaffolds after culturing for 1, 3, 5 and 7 days (n = 3, mean ± SD, *P < 0.05 vs CS group; **P < 0.01 vs CS group). (b) Fluorescence microscopic inspection of cells cultured with the CS group and Sr-CS group for 1, 3, 5 and 7 days (AO/EB staining). The scale bars are 100 μm. The fluorescence microscopic images were taken after staining the nuclei (blue) and actin filaments (red) in both groups of samples for 3 days to observe the precise morphology of cells. The scale bars are 10 μm. (c) ALP activity of rBMSCs distributed on different collagen scaffolds after culturing for 7 and 14 days. (n = 3, mean ± SD, *P < 0.05 vs CS group; **P < 0.01 vs CS group). (d,e) The relative mRNA levels of osteogenesis-related genes (RUNX2, OCN, ALP) in rBMSCs cultured in different groups for 7 days and 14 days (n = 3, mean ± SD, *P < 0.05 vs CS group; **P < 0.01 vs CS group).

calculated BV/TV values from *in vivo* evaluations. The results showed that among all groups, new bone formation was most marked in the Sr-CS group at the macro level. After 1 month, the BV/TV value in the Sr-doped group was 28.07 ± 1.25%, while new bone matrix formation could not be observed in the blank and control groups. After 2, 3, and 6 months, the BV/TV values in the Sr-doped group were 41.37 ± 2.08%, 64.17 ± 1.2%, and 66.57 ± 0.77%, respectively, which were significantly higher than in the other two groups (P < 0.05).

We mainly utilized two kinds of histological staining to observe the differences among the three scaffolds *in vivo* at the histological level (Fig. 8a and b). The purplish red colour of tissue stained with H&E and Masson's trichrome indicated bone matrix composed of uniform acidophilic tissue, and new bone formation was revealed by the uniform, dark blue colour, which confirmed the micro-CT results. To confirm the inflammatory cell infiltration and distribution around the different implanted biomaterials, tissue sections from the rat calvarial defect model were immunostained with CD68+ (Fig. 8c). Analysis of the stain results from the above classes of indicators revealed the actual *in vivo* inflammation and bone formation due to introduction of the scaffold materials. Osteoid formation with osteoblasts and the initiation of capillary vessels could be well observed after the first month in the Sr-doped group, showing the potential for osteoinduction. These structures were hardly observed in the control groups. By contrast, H&E staining revealed that a greater amount of fibrous connective tissue surrounded the CS-filled defect and the defect in the blank group than the Sr-CS-filled defect at 1, 2, and 3 months. Masson's trichrome staining of specimens revealed the same results as H&E staining. Additionally, as shown by H&E staining, a reduced macrophage (CD68-positive cells) distribution and proportion was observed in the Sr-CS group than in the

blank and control groups (P < 0.01), and the blank and CS groups exhibited a similar inflammatory response at 1 and 2 months. Inflammatory cells were significantly more scattered in the tissues in the blank and CS groups than the Sr-CS group. Due to the long-term growth and repair process, there was no significant difference in the staining results obtained for the three groups of samples at 3 and 6 months. These *in vivo* investigations verified that Sr-CS resulted in a less severe immune response than CS and enabled satisfactory regeneration of bone tissue.

4. Discussion

The essence of biomineralization is the mineralization of organic matrices, which involves the self-assembly of minerals and organic matrices in a temporal and spatial context. Typical organic matrices mainly include chitin, collagen, and amelogenin, and inorganic components mainly include calcium carbonate and calcium phosphates [12,34]. Specifically, there are a variety of noncalcific biominerals, such as biosilica in diatoms [35], iron oxides in chiton, and limpet teeth [36], and an uncommon copper hydroxide in the teeth-like jaws of a bloodworm [37]. These special cases have inspired scientists and engineers to develop a noncalcific collagen matrix that exhibits specific functions. A representative case is the development of silicified collagen matrices for bone regeneration applications, which was achieved through the infiltration of choline-stabilized silicic acid (Ch–SA) into polyallylamine (PAH)-enriched type I collagen via the gap zones [30]. Since the self-assembly of collagen was carried out before silification, this method could be classified as an MFS model. This methodology is specific for stabilizing silicic acid but not other amorphous mineral salts
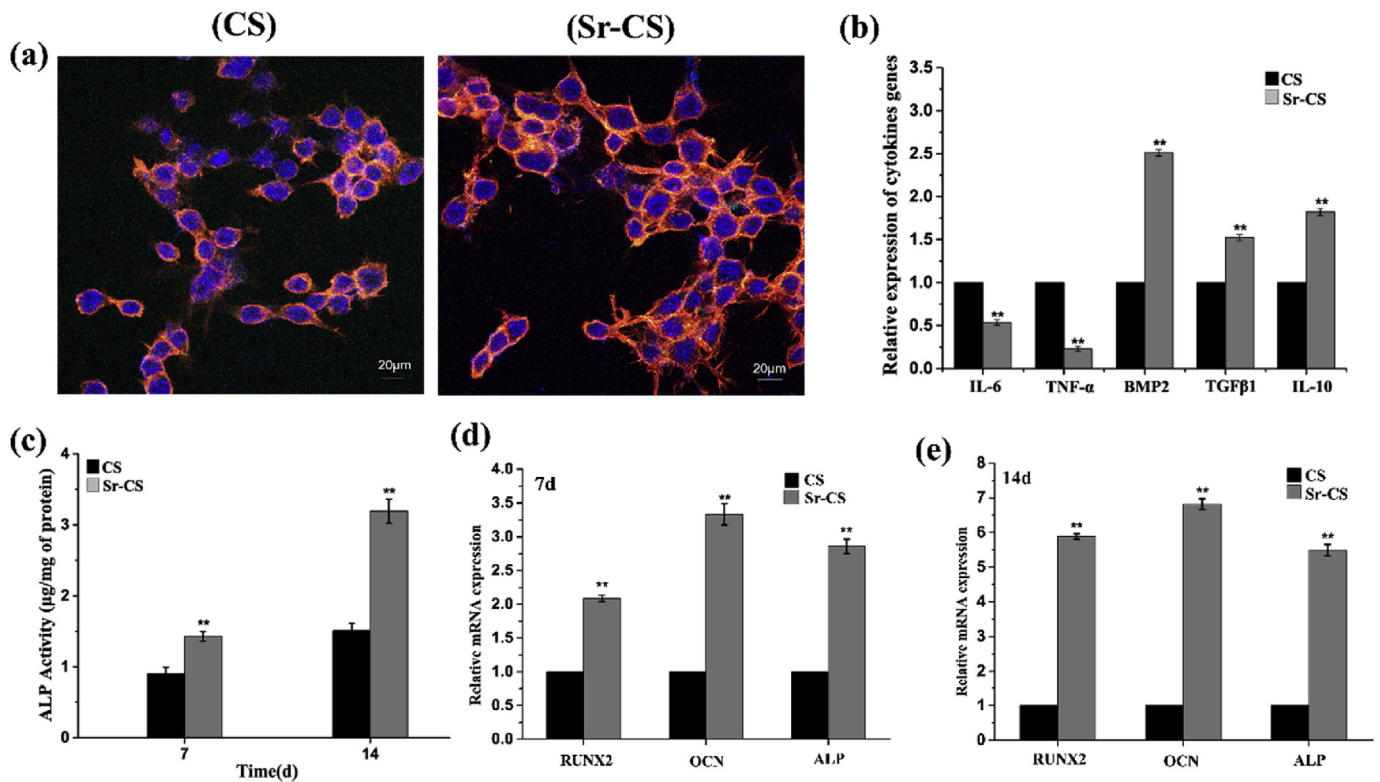
Fig. 6. (a) Fluorescence microscopic images of RAW264.7 cells obtained after staining nuclei (blue) and actin filaments (red). RAW264.7 cells cultured with the CS group and Sr-CS group for 2 days. The scale bars are 20 μm (b) The relative mRNA levels of cytokines and osteogenic-related genes of RAW 264.7 cells stimulated by macrophage-conditioned CS and Sr−CS for 3 days. (c) ALP activity of rBMSCs distributed in different macrophage-conditioned media after culturing for 7 and 14 days (n = 3, mean ± SD, *$P < 0.05$ vs CS group; **$P < 0.01$ vs CS group). (d,e) The relative mRNA levels of osteogenesis-related genes (RUNX2, OCN, ALP) in rBMSCs cultured in different macrophage-conditioned medium groups for 7 days and 14 days (n = 3, mean ± SD, *$P < 0.05$ vs CS group; **$P < 0.01$ vs CS group).

for which the introduction of various elements into collagen may not be feasible.

In this study, we attempted to introduce various amorphous minerals into collagen self-assembled by the SSM model, by which various bioactive elements could be doped into the collagen scaffolds. Since *in vitro* self-assembly of collagen starts under acidic conditions [38], the presence of CMC, a polyampholyte that can stabilize various amorphous mineral salts below pH 3.5, is a precondition for the SSM model.

In acidic environments, most mineral salts will essentially be ionized and thus completely dissolve, and carbonate or phosphate is protonated in solution. Thermodynamic prediction suggests the precipitation or ionization of supersaturated cationic mineral ions and acid radicals under neutral environment or alkaline, or acidic environments, respectively. However, our present findings showed that in addition to ACP, CMC was able to stabilize various nanoparticles of amorphous carbonates or phosphates, including ASC and amorphous magnesium
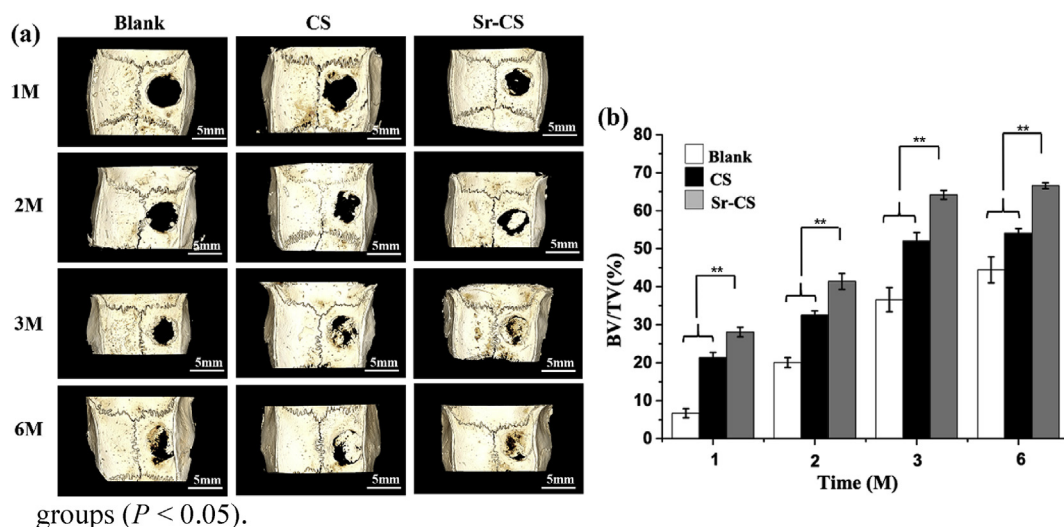

groups ($P < 0.05$).

Fig. 7. (a) Reconstructed 3D micro-CT images of new bone regeneration at 1, 2, 3 and 6 months post-operation. The scale bars are 5 mm. (b) Quantitative analysis of regenerated bone in values of BV/TV for the control group and groups filled with CS or Sr-CS (n = 3, mean ± SD, **$P < 0.01$ vs Sr-CS group).
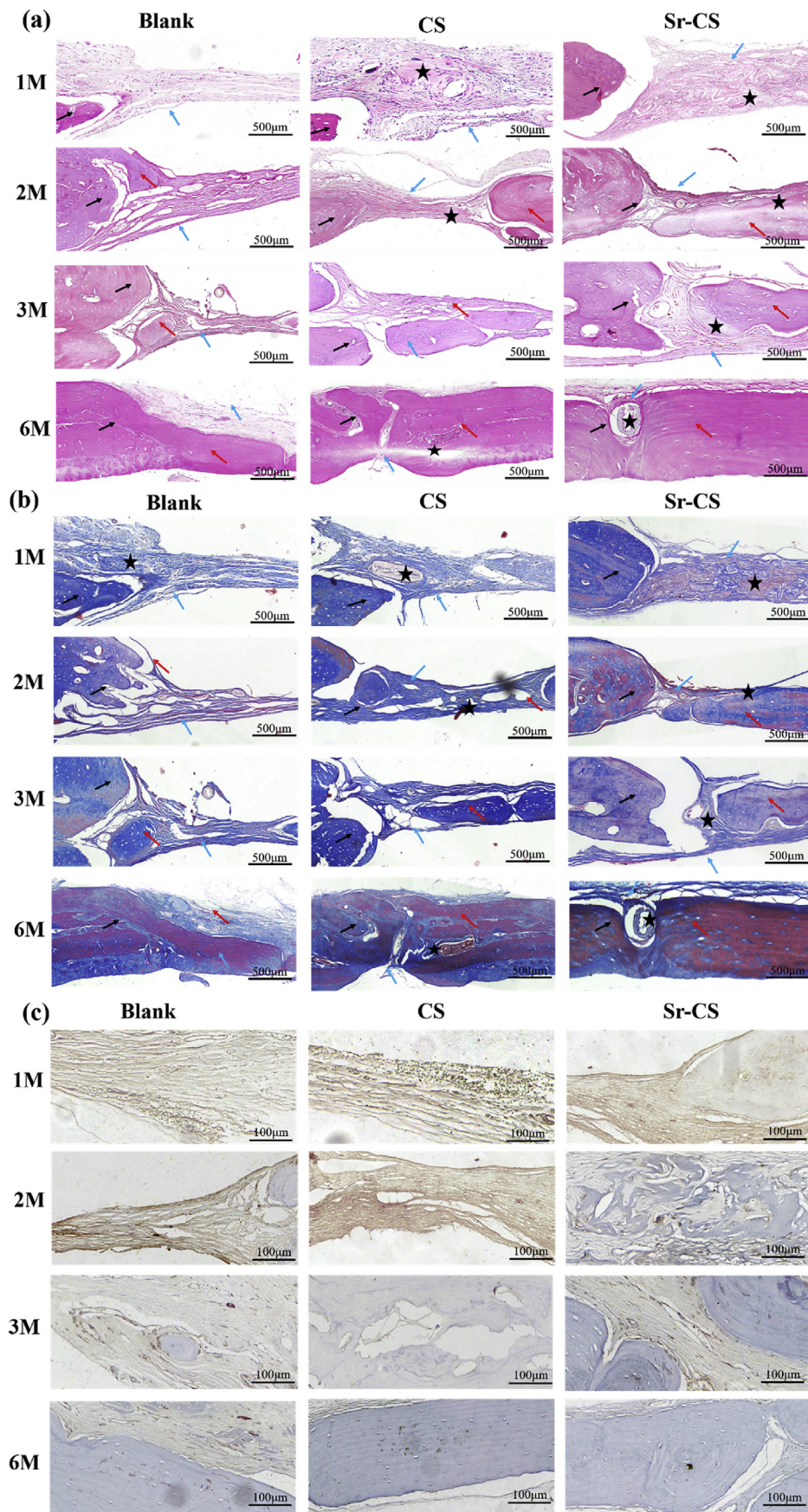
Fig. 8. (a,b) Histological analysis of bone formation at 1, 2, 3, and 6 months by H&E and Masson's trichrome staining of rat cranial defects and surrounding tissue at different test times: blank control, filled with CS, and filled with Sr-CS. (black arrows, host bone; red arrows, new bone; black stars, osteoid; blue arrows, fibrous tissue). The scale bars are 500 μm. (c) Immunohistochemical staining for CD68$^+$ cells in the three groups at 1, 2, 3, and 6 months. The scale bars are 100 μm.
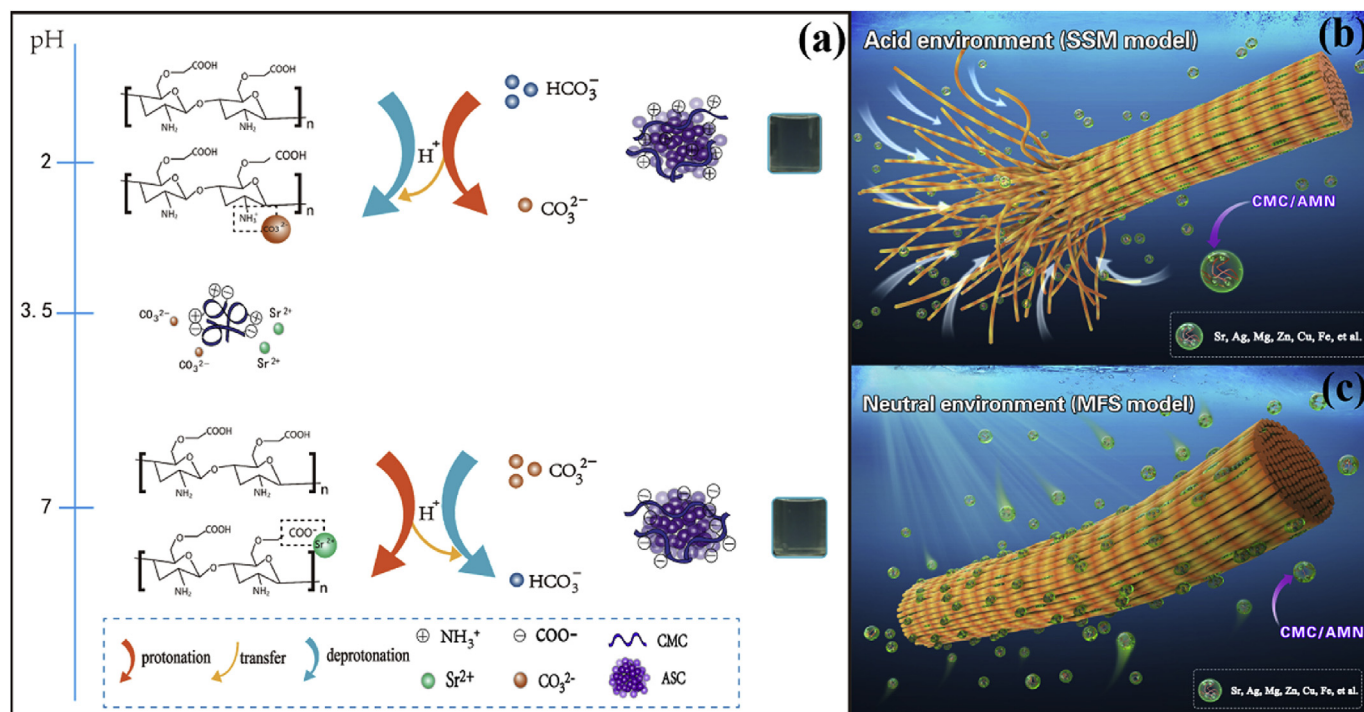
Fig. 9. (a) Schematic diagram showing the interactions between CMC, metal cations and acid radicals. At pH 7, with protonation of HCO3-, ASC can be stabilized by the acidic polymer CMC. In contrast, at pH 2, CMC competes with mineral anions for protonation, thereby causing deprotonation of the mineral anions to a certain degree to form ASC. (b) Schematic diagram showing that various bioactive elements were incorporated into collagen fibrils via the SSM model. In this model, the amorphous mineral nanoparticles are first stabilized by CMC and then mixed and interacted with the collagen microfibrils. With further collagen self-assembly, nanoparticles are trapped and localized in the gap zones. (c) Schematic diagram showing various bioactive elements aggregated on the surfaces of collagen fibrils via the MFS model.

phosphate, among others, at both pH 2 and pH 7 (Supporting Information S1). A potential barrier to the crystallization of amorphous minerals in solution is related to the degrees of freedom of the carbonate or phosphate anions (e.g., rotational, tilting and protonation) (Fig. 9a) [17]. Under neutral or alkaline conditions, this barrier can be increased by the introduction of additional degrees of freedom from the addition of acidic polymers (in addition to the reduction in supersaturation of the mineralization solution from the sequestration of cations by negatively charged acidic polymers), which would reduce the symmetry of carbonate or phosphate and amplify the effect via protonation of those anions as HCO_3^- or HPO_4^{2-}. The same rationale can be applied for the stabilization of amorphous minerals with CMC as an acidic polymer at pH 7 [39]. In contrast, at pH 2, the protonation of carbonate or phosphate is dominant, indicating a dissolution tendency of the minerals; thus, deprotonation of the mineral anions is required to weaken the trend of ionization between mineral cations and anions for the formation of ACP. CMC at pH 2 competes with mineral anions for protons, causing a certain degree of deprotonation of the mineral anions to facilitate the deposition of mineral cations and anions (forming ACP). Cleverly, this deposition tendency is appropriately inhibited by sequestering cations using positively charged CMC, balancing the interactions among CMC, mineral cations, and acid radicals, and thereby, maintaining an emulsified state of the solution containing amorphous mineral nanoparticles at pH 2. Accordingly, with the help of CMC, nanoparticles of ASC, amorphous magnesium carbonate, amorphous zinc phosphate, amorphous iron phosphate, amorphous silver phosphate (ASP), and amorphous copper phosphate were incorporated into collagen fibrils via the SSM model. An increase in pH to neutral or alkaline (deprotonation tendency) conditions can convert the ASC nanoparticles to strontium carbonate crystals (strontianite crystallites), similar to the transformation from ACP to HAP. This rationale is consistent with other mineral transformations from the amorphous phase to the crystalline state in the present study. This process is described in

the illustration shown in Fig. 9b.

In the MFS model (Fig. 9c), due to the screening at the gap zones (size-exclusion effect) [9], the polymers stabilizing ACP are not able to enter the collagen fibrils, and small and dispersed ACP nanoparticles as prenucleation clusters are likely to infiltrate the self-assembled collagen, with such infiltration potentially driven by the balance between osmotic equilibrium and electroneutrality [8]; substantially, this process represents a migration of ACP nanoparticles from a polymer matrix to a collagen matrix. Unlike acidic conditions, neutral or alkaline conditions cause ACP nanoparticles to be less thermodynamically and kinetically stable, which leads to the formation of large and dense nanoparticles due to the aggregation tendency (Fig. 1a). These amorphous minerals cannot enter the self-assembled collagen fibrils, and their aggregations on the surfaces of collagen may block the gap zones and thus inhibit the infiltration of other smaller nanoparticles [40]. Thus, in this study, the efficacy of doping with bioactive elements was lower using the MFS model than the SSM model.

In summary, in the SSM model, the amorphous mineral nanoparticles stabilized by CMC and the collagen molecules were both primary components; as the pH gradually increased, the collagen molecules began to self-assemble into collagen fibrils in the presence of amorphous mineral nanoparticles. Here, dialysis caused a slow increase in pH in the SSM model, which provides sufficient time for the assembly of collagen molecules and nanoparticles. The TEM results indicated that this effect could be a self-adaptive interaction between the amorphous mineral nanoparticles and collagen microfibrils, in which the nanoparticles were wrapped and squeezed by the collagen microfibrils and the nanoparticles between the collagen microfibrils would adopt spindle shapes with a length of approximately 40 nm corresponding to the gap region of the collagen along the long axis of the collagen microfibrils. The amorphous mineral nanoparticles could then fuse, extend and transform into mineral crystals to achieve the intrafibrillar mineralization of collagen.

Collagen scaffolds that mimic the natural extracellular matrix provide structural support for cells in a 3D environment. However, compared with the extracellular matrix, pure collagen scaffolds lack proper exogenous and endogenous osteogenic factors and osteoimmunomodulatory ability [41,42]. In this study, the representative element strontium (Sr), possessing osteoconductive and osteoimmunomodulatory properties, was doped into collagen through the SSM model, and this scaffold exhibited sustained release of Sr^{2+} that differed from the significant initial burst release of Sr^{2+} from the scaffold built by the MFS model (Fig. 3c–f). In addition, the Sr-CS generated by the immediate co-precipitation of collagen fibrils and apatite minerals doped with Sr (i.e., the collagen/apatite self-assembly model) led to more extrafibrillar mineralization of collagen, showing a burst release of Sr^{2+} [29]. Since the collagen matrix works as a steric barrier to retard the diffusion of mineral ions, the intrafibrillar mineralized scaffolds are prone to a sustained release of mineral ions. Thus, the release profiles of mineral ions indirectly indicated the higher intrafibrillar mineralization efficiency using the SSM model.

It has been well documented that strontium activates multiple signalling pathways to act on osteoblasts and osteoclasts, and regulates bone formation and resorption at the cellular and molecular levels, thereby increasing bone mineral density and enhancing bone stiffness and osteoinductive capacity [43–45]. In this study, rBMSCs cultured on Sr-CS or CS proliferated gradually over the culture time, showing no negative effect on the attachment and proliferation of rBMSCs, thus indicating their *in vitro* biocompatibility and noncytotoxicity. Interestingly, rBMSCs cultured on Sr-CS displayed significantly higher expression levels of osteogenesis-related genes (RUNX2, OCN, ALP) and ALP activity than those cultured on CS (Fig. 5). Therefore, the strontium ions released from the scaffolds fabricated by the SSM model could promote osteogenesis of BMSCs *in vitro*.

Most importantly, it has been recognized that the inconsistencies between *in vitro* and *in vivo* evaluations of biomaterials are due to the response of osteoblastic lineage cells and the neglect of the role of immune cells [46–48]. Due to the multi-directional effects of macrophages on the dynamic flux of bone formation and homeostasis, the response of macrophages to bone biomaterials has become the subject of much interest in the evaluation of osteoimmunomodulatory properties [49,50]. Accordingly, we tested the *in vitro* osteogenic capacity of Sr-CS with the novel approach of including macrophages. Macrophages can be polarized towards different phenotypes in response to their microenvironment. Having been activated with the M1 phenotype, M1 macrophages can produce pro-inflammatory mediators (TNF-α, IL-6, and IL-1β) that contribute to the progression of inflammation; by contrast, when polarized to the M2 phenotype, M2 macrophages tend to secrete various anti-inflammatory cytokines (IL-10 and TGFβ1), resulting in wound healing [51,52]. In this study, the expression levels of pro-inflammatory factors in macrophages on Sr-CS were lower than on CS, and Sr-CS exhibited greater osteogenetic potential according to the osteogenesis-related gene expression (Fig. 6). The potential mechanism appeared to consist of strontium ion regulation of immune status by suppressing IL-6 and TNF-a expression in macrophages, which actually stimulate transduction pathways that lead to the activation of nuclear factor kappa-light-chain-enhancer of activated B cells (NFκB). Strontium released from scaffolds stimulated the appropriate process of macrophage polarization from M1 to M2. The inflammatory role of NFκB has been antagonized, suggesting the anti-inflammatory effect of strontium. These results are consistent with a previous study in which macrophage responses were modulated with strontium-substituted submicrometer bioactive glass [53]. Moreover, biomaterials could mediate the osteogenic differentiation of BMSCs by BMP2 and TGF-β1 expressed and secreted from macrophages [54,55]. In this study, the high level of BMP2 and TGF-β1 gene expression stimulated by Sr confirmed the improved osteogenetic and immunoregulatory effects of Sr-CS. However, to evaluate osteogenesis stimulated by bone biomaterials, a systemic study is required to determine whether bioactive ions can

synergistically stimulate bone regeneration, and more detailed immune responses are needed to investigate the involvement of other immunocytes.

Having demonstrated the osteogenetic potential of Sr-CS *in vitro*, we next used a rat calvarial defect model to examine the *in vivo* therapeutic effect of the collagen scaffolds on osteogenesis. To monitor the formation of bone tissue, histological and microradiography studies were performed on the specimens after different implantation periods. The micro-CT results illustrated more new bone regeneration in the Sr-CS group than the CS group. The BV/TV value achieved was higher in the Sr-CS group (66.57 ± 0.77%) than the CS group (54.10 ± 1.20%) and blank group (44.40 ± 3.40%) at 6 months post-operation (Fig. 7). Histological analysis and immunohistochemical staining of $CD68^+$ cells from the rat cranial defect and surrounding tissue at different testing times showed no signs of foreign-body reactions or acute inflammation, and preferable bone formation was observed in the Sr-CS group (Fig. 8). Both the microradiography and histological analysis results indicated that Sr-CS showed better biocompatibility and osteoinductivity; presenting less inflammation than the other scaffolds, Sr-CS acted as a potential immunomodulatory material for improved bone regeneration.

In the present study, we presented the development of a multifunctional scaffold that with osteogenetic and antibacterial properties. Silver-based products have shown to be promising candidates for antimicrobial and anti-inflammatory materials that also have low systemic toxicity. Currently, silver colloid-loaded collagen sponges (typically Gelatamp) [56] are used in periodontal bone grafting or dental implant surgery to avoid surgical infections caused by pathogenic bacteria. Herein, we found that by using the SSM model, the incorporation of Ag^+ resulted in an antibacterial scaffold that also showed sustained release of Ag^+. Free Ag^+ ions have an inherent antimicrobial effect by disrupting cell membranes and disturbing permeability and respiration. These ions can also bind to microbial DNA and sulfhydryl groups of the metabolic enzymes of bacteria, resulting in bacterial inactivation [23,57,58]. Ag-CS resulted in a significant reduction of *S. aureus* growth in comparison to the collagen control at 3 days (Fig. 4). Therefore, the SSM model provides a new methodology for loading silver into collagen.

5. Conclusion

In this study, collagen scaffolds with osteogenic, immunomodulatory and antibacterial properties for bone tissue engineering were successfully fabricated via the SSM model. Compared with other methods, the SSM model achieved high-efficiency loading of bioactive elements and sustained release of these elements. Based on *in vitro* and *in vivo* biological assessments, Sr-CS showed significantly improved osteogenesis of rBMSCs and modulated the macrophage response to achieve an improved effect on bone regeneration, and Ag-CS exhibited excellent antibacterial effects against *S. aureus*. Therefore, the SSM model represents a de novo synthetic strategy for doping various bioactive elements into collagen; using this approach, multifunctional collagen scaffolds could be fabricated to meet the clinical challenges of encouraging osteogenesis, boosting the immune response and fighting severe infection in bone defects. The development and investigation of multiple bioactive element-doped collagen scaffolds will be carried out in the future.

CRediT authorship contribution statement

Huanhuan Liu: Investigation, Writing - original draft. **Mingli Lin:** Investigation, Writing - original draft. **Xue Liu:** Formal analysis. **Ye Zhang:** Validation. **Yuyu Luo:** Resources. **Yanyun Pang:** Conceptualization, Investigation. **Haitao Chen:** Formal analysis. **Dongwang Zhu:** Validation. **Xue Zhong:** Conceptualization, Investigation. **Shiqing Ma:** Conceptualization, Investigation. **Yanhong Zhao:** Data curation. **Qiang Yang:** Supervision. **Xu Zhang:**

Conceptualization, Methodology, Writing - review & editing.

Appendix A. Supplementary data

Supplementary data to this article can be found online at https://doi.org/10.1016/j.bioactmat.2020.06.005.

References

[1] W. Zhang, S.S. Liao, F.Z. Cui, Hierarchical self-assembly of nano-fibrils in mineralized collagen, Chem. Mater. 15 (16) (2003) 3221–3226.

[2] T. Du, X. Niu, Z. Li, P. Li, Q. Feng, Y. Fan, Crosslinking induces high mineralization of apatite minerals on collagen fibers, Int. J. Biol. Macromol. 113 (2018) 450–457.

[3] M. Lin, H. Liu, J. Deng, R. An, M. Shen, Y. Li, X. Zhang, Carboxymethyl chitosan as a polyampholyte mediating intrafibrillar mineralization of collagen via collagen/ACP self-assembly, J. Mater. Sci. Technol. 35 (9) (2019) 1894–1905.

[4] Z. Chen, S. Cao, H. Wang, Y. Li, A. Kishen, X. Deng, X. Yang, Y. Wang, C. Cong, H. Wang, X. Zhang, Biomimetic remineralization of demineralized dentine using scaffold of CMC/ACP nanocomplexes in an in vitro tooth model of deep caries, PloS One 10 (1) (2015) e0116553.

[5] F. Nudelman, K. Pieterse, A. George, P.H. Bomans, H. Friedrich, L.J. Brylka, P.A. Hilbers, G. de With, N.A. Sommerdijk, The role of collagen in bone apatite formation in the presence of hydroxyapatite nucleation inhibitors, Nat. Mater. 9 (12) (2010) 1004–1009.

[6] A. Tsortos, G.H. Nancollas, The role of polycarboxylic acids in calcium phosphate mineralization, J. Colloid Interface Sci. 250 (1) (2002) 159–167.

[7] F.R. Tay, D.H. Pashley, Guided tissue remineralisation of partially demineralised human dentine, Biomaterials 29 (8) (2008) 1127–1137.

[8] L.N. Niu, S.E. Jee, K. Jiao, L. Tonggu, M. Li, L. Wang, Y.D. Yang, J.H. Bian, L. Breschi, S.S. Jang, J.H. Chen, D.H. Pashley, F.R. Tay, Collagen intrafibrillar mineralization as a result of the balance between osmotic equilibrium and electroneutrality, Nat. Mater. 16 (3) (2017) 370–378.

[9] D. Toroian, J.E. Lim, P.A. Price, The size exclusion characteristics of type I collagen: implications for the role of noncollagenous bone constituents in mineralization, J. Biol. Chem. 282 (31) (2007) 22437–22447.

[10] M. Takahashi, M. Nakajima, J. Tagami, D.L.S. Scheffel, R.M. Carvalho, A. Mazzoni, M. Cadenaro, A. Tezvergil-Mutluay, L. Breschi, L. Tjäderhane, S.S. Jang, F.R. Tay, K.A. Agee, D.H. Pashley, The importance of size-exclusion characteristics of type I collagen in bonding to dentin matrices, Acta Biomater. 9 (12) (2013) 9522–9528.

[11] M.J. Olszta, D.J. Odom, E.P. Douglas, L.B. Gower, A new paradigm for biomineral formation: mineralization via an amorphous liquid-phase precursor, Connect. Tissue Res. 44 (1) (2009) 326–334.

[12] S.T. Li, E.P. Katz, An electrostatic model for collagen fibrils. The interaction of reconstituted collagen with Ca++, Na+, and Cl, Biopolymers 15 (8) (1976) 1439–1460.

[13] T. Cate, A. R, Oral Histology Development, Structure, and Function, fourth, 1994.

[14] E. Beniash, J.P. Simmer, H.C. Margolis, The effect of recombinant mouse amelogenins on the formation and organization of hydroxyapatite crystals in vitro, J. Struct. Biol. 149 (2) (2005) 182–190.

[15] L. Chen, Z. Tian, Y. Du, Synthesis and pH sensitivity of carboxymethyl chitosan-based polyampholyte hydrogels for protein carrier matrices, Biomaterials 25 (17) (2004) 3725–3732.

[16] A. Ciferri, S. Kudaibergenov, Natural and synthetic polyampholytes, 1, Macromol. Rapid Commun. 28 (20) (2007) 1953–1968.

[17] S.E. Wolf, L. Muller, R. Barrea, C.J. Kampf, J. Leiterer, U. Panne, T. Hoffmann, F. Emmerling, W. Tremel, Carbonate-coordinated metal complexes precede the formation of liquid amorphous mineral emulsions of divalent metal carbonates, Nanoscale 3 (3) (2011) 1158–1165.

[18] F. Yang, D. Yang, J. Tu, Q. Zheng, L. Cai, L. Wang, Strontium enhances osteogenic differentiation of mesenchymal stem cells and in vivo bone formation by activating Wnt/catenin signaling, Stem Cell. 29 (6) (2011) 981–991.

[19] L. Claes, S. Recknagel, A. Ignatius, Fracture healing under healthy and inflammatory conditions, Nat. Rev. Rheumatol. 8 (3) (2012) 133–143.

[20] P. Guihard, Y. Danger, B. Brounais, E. David, R. Brion, J. Delecrin, C.D. Richards, S. Chevalier, F. Redini, D. Heymann, H. Gascan, F. Blanchard, Induction of osteogenesis in mesenchymal stem cells by activated monocytes/macrophages depends on oncostatin M signaling, Stem Cell. 30 (4) (2012) 762–772.

[21] N. Mokarram, R.V. Bellamkonda, A perspective on immunomodulation and tissue repair, Ann. Biomed. Eng. 42 (2) (2014) 338–351.

[22] S. Panzavolta, P. Torricelli, S. Casolari, A. Parrilli, M. Fini, A. Bigi, Strontium-substituted hydroxyapatite-gelatin biomimetic scaffolds modulate bone cell response, Macromol. Biosci. 18 (7) (2018) e1800096.

[23] B. Le Ouay, F. Stellacci, Antibacterial activity of silver nanoparticles: a surface science insight, Nano Today 10 (3) (2015) 339–354.

[24] S. Eckhardt, P.S. Brunetto, J. Gagnon, M. Priebe, B. Giese, K.M. Fromm, Nanobio silver: its interactions with peptides and bacteria, and its uses in medicine, Chem. Rev. 113 (7) (2013) 4708–4754.

[25] F.Z. Cui, Y. Li, J. Ge, Self-assembly of mineralized collagen composites, Mater. Sci. Eng. R Rep. 57 (1–6) (2007) 1–27.

[26] J.-H. Bradt, M. Mertig, A. Teresiak, W. Pompe, Biomimetic mineralization of collagen by combined fibril assembly and calcium phosphate formation, Chem. Mater. 11 (10) (1999) 2694–2701.

[27] Y. Wang, N. Van Manh, H. Wang, X. Zhong, X. Zhang, C. Li, Synergistic intrafibrillar/extrafibrillar mineralization of collagen scaffolds based on a biomimetic strategy to promote the regeneration of bone defects, Int. J. Nanomed. 11 (2016) 2053–2067.

[28] Y. Wang, Y. Hua, Q. Zhang, J. Yang, H. Li, Y. Li, M. Cao, Q. Cai, X. Yang, X. Zhang, C. Li, Using biomimetically mineralized collagen membranes with different surface stiffness to guide regeneration of bone defects, J. Tissue Eng. Regen. Med. 12 (7) (2018) 1545–1555.

[29] M. Quade, M. Schumacher, A. Bernhardt, A. Lode, M. Kampschulte, A. Voss, P. Simon, O. Uckermann, M. Kirsch, M. Gelinsky, Strontium-modification of porous scaffolds from mineralized collagen for potential use in bone defect therapy, Mater. Sci. Eng. C Mater. Biol. Appl. 84 (2018) 159–167.

[30] L.N. Niu, K. Jiao, Y.P. Qi, C.K. Yiu, H. Ryou, D.D. Arola, J.H. Chen, L. Breschi, D.H. Pashley, F.R. Tay, Infiltration of silica inside fibrillar collagen, Angew Chem. Int. Ed. Engl. 50 (49) (2011) 11688–11691.

[31] L.M. Delgado, A. Pandit, D.I. Zeugolis, Influence of sterilisation methods on collagen-based devices stability and properties, Expet Rev. Med. Dev. 11 (3) (2014) 305–314.

[32] W. Zhang, Z.L. Huang, S.S. Liao, F.Z. Cui, Nucleation sites of calcium phosphate crystals during collagen mineralization, J. Am. Ceram. Soc. 86 (6) (2003) 1052–1054.

[33] Y. Zhai, F.Z. Cui, Y. Wang, Formation of nano-hydroxyapatite on recombinant human-like collagen fibrils, Curr. Appl. Phys. 5 (5) (2005) 429–432.

[34] H. Ehrlich, Chitin and collagen as universal and alternative templates in biomineralization, Int. Geol. Rev. 52 (7–8) (2010) 661–699.

[35] R. Ragni, S. Cicco, D. Vona, G. Leone, G.M. Farinola, Biosilica from diatoms microalgae: smart materials from bio-medicine to photonics, J. Mater. Res. 32 (2) (2016) 279–291.

[36] D. Joester, L.R. Brooker, The Chiton Radula: A Model System for Versatile Use of Iron Oxides, in: D. Faivre (Ed.), Iron Oxides: From Nature to Applications, Wiley-VCH Verlag GmbH & Co. KGaA, Weinheim, Germany, 2016, pp. 177–205.

[37] H.C. Lichtenegger, T. Schoberl, M.H. Bartl, H. Waite, G.D. Stucky, High abrasion resistance with sparse mineralization: copper biomineral in worm jaws, Science 298 (5592) (2002) 389–392.

[38] Y. Wang, T. Azais, M. Robin, A. Vallee, C. Catania, P. Legriel, G. Pehau-Arnaudet, F. Babonneau, M.M. Giraud-Guille, N. Nassif, The predominant role of collagen in the nucleation, growth, structure and orientation of bone apatite, Nat. Mater. 11 (8) (2012) 724–733.

[39] R. Wang, J. Guo, X. Lin, S. Chen, S. Mai, Influence of molecular weight and concentration of carboxymethyl chitosan on biomimetic mineralization of collagen, RSC Adv. 10 (22) (2020) 12970–12981.

[40] H. Colfen, S. Mann, Higher-order organization by mesoscale self-assembly and transformation of hybrid nanostructures, Angew Chem. Int. Ed. Engl. 42 (21) (2003) 2350–2365.

[41] Y. Li, Y. Xiao, C. Liu, The horizon of materiobiology: a perspective on material-guided cell behaviors and tissue engineering, Chem. Rev. 117 (5) (2017) 4376–4421.

[42] V. Hernandez-Gordillo, J. Chmielewski, Mimicking the extracellular matrix with functionalized, metal-assembled collagen peptide scaffolds, Biomaterials 35 (26) (2014) 7363–7373.

[43] J. Braux, F. Velard, C. Guillaume, S. Bouthors, E. Jallot, J.M. Nedelec, D. Laurent-Maquin, P. Laquerriere, A new insight into the dissociating effect of strontium on bone resorption and formation, Acta Biomater. 7 (6) (2011) 2593–2603.

[44] Z. Saidak, P.J. Marie, Strontium signaling: molecular mechanisms and therapeutic implications in osteoporosis, Pharmacol. Ther. 136 (2) (2012) 216–226.

[45] S. Kumar, K. Chatterjee, Strontium eluting graphene hybrid nanoparticles augment osteogenesis in a 3D tissue scaffold, Nanoscale 7 (5) (2015) 2023–2033.

[46] J.R. Arron, Y. Choi, Bone versus immune system, Nature 408 (6812) (2000) 535–536.

[47] H. Takayanagi, Osteoimmunology: shared mechanisms and crosstalk between the immune and bone systems, Nat. Rev. Immunol. 7 (4) (2007) 292–304.

[48] S. Franz, S. Rammelt, D. Scharnweber, J.C. Simon, Immune responses to implants - a review of the implications for the design of immunomodulatory biomaterials, Biomaterials 32 (28) (2011) 6692–6709.

[49] Z. Chen, T. Klein, R.Z. Murray, R. Crawford, J. Chang, C. Wu, Y. Xiao, Osteoimmunomodulation for the development of advanced bone biomaterials, Mater. Today 19 (6) (2016) 304–321.

[50] Z. Chen, J. Yuen, R. Crawford, J. Chang, C. Wu, Y. Xiao, The effect of osteoimmunomodulation on the osteogenic effects of cobalt incorporated beta-tricalcium phosphate, Biomaterials 61 (2015) 126–138.

[51] F. Wei, Y. Zhou, J. Wang, C. Liu, Y. Xiao, The immunomodulatory role of BMP-2 on macrophages to accelerate osteogenesis, Tissue Eng. A 24 (7–8) (2018) 584–594.

[52] C.D. Mills, K. Kincaid, J.M. Alt, M.J. Heilman, A.M. Hill, M-1/M-2 macrophages and the Th1/Th2 paradigm, J. Immunol. 164 (12) (2000) 6166–6173.

[53] W. Zhang, F. Zhao, D. Huang, X. Fu, X. Li, X. Chen, Strontium-substituted submicrometer bioactive glasses modulate macrophage responses for improved bone regeneration, ACS Appl. Mater. Interfaces 8 (45) (2016) 30747–30758.

[54] Z. Chen, C. Wu, W. Gu, T. Klein, R. Crawford, Y. Xiao, Osteogenic differentiation of bone marrow MSCs by beta-tricalcium phosphate stimulating macrophages via

[55] BMP2 signalling pathway, Biomaterials 35 (5) (2014) 1507–1518.

[55] C.M. Champagne, J. Takebe, S. Offenbacher, L.F. Cooper, Macrophage cell lines produce osteoinductive signals that include bone morphogenetic protein-2, Bone 30 (1) (2002) 26–31.

[56] C. You, Q. Li, X. Wang, P. Wu, J.K. Ho, R. Jin, L. Zhang, H. Shao, C. Han, Silver nanoparticle loaded collagen/chitosan scaffolds promote wound healing via regulating fibroblast migration and macrophage activation, Sci. Rep. 7 (1) (2017) 10489.

[57] K. Zheng, M.I. Setyawati, D.T. Leong, J. Xie, Antimicrobial silver nanomaterials, Coord. Chem. Rev. 357 (2018) 1–17.

[58] M. Rai, A. Yadav, A. Gade, Silver nanoparticles as a new generation of antimicrobials, Biotechnol. Adv. 27 (1) (2009) 76–83.